As per UGC guidelines an electronic bar code is provided to secure your paper

International Journal for Modern Trends in Science and Technology
Volume 12, Issue 08, pages 80-93.
ISSN: 2455-3778 online
Available online at: http://www.ijmtst.com/vol12issue06.html
DOI: https://doi.org/10.5281/zenodo.22151964

ANFIS Based DC-Link Voltage Regulation and Energy Management in Grid-Interactive PV-Wind-Battery EV Integrated DC Microgrid

Kartheek Battula | M. Lokanadham | Dr. K. Siva Kumar

Department of Electrical & Electronics Engineering, Sri Venkatesa Perumal College of Engineering and Technology, Puttur, Andhra Pradesh, India.

To Cite this Article
Kartheek Battula, M. Lokanadham & Dr. K. Siva Kumar (2026). ANFIS Based DC-Link Voltage Regulation and Energy Management in Grid-Interactive PV-Wind-Battery EV Integrated DC Microgrid. International Journal for Modern Trends in Science and Technology, 12(08), 80-93. https://doi.org/10.5281/zenodo.22151964

Article Info
Received: 28 July 2026; Revised: 16 August 2026; Accepted: 20 July 2026.

KEYWORDS

ANFIS controller, bidirectional DC-DC converter, DC microgrid, electric vehicle (EV) charging, energy management, grid-interfaced converter, power quality

ABSTRACT

The rapid integration of renewable energy sources (RESs), battery energy storage systems (BESSs), and electric vehicle (EV) charging infrastructure into grid-interactive DC microgrids presents complex challenges for DC-link voltage stability and power quality. This paper proposes a sophisticated Adaptive Neuro-Fuzzy Inference System (ANFIS)-based control strategy for a PV-wind-battery-EV integrated DC microgrid. The system architecture features a bidirectional DC-DC converter at the DC bus side to manage EV charging and facilitate vehicle-to-grid (V2G) power exchange, alongside a similar interface for controlled battery operation. To ensure resilience under distorted grid conditions, the proposed method utilizes an Anti-Windup Mixed-Order Generalized Integrator (AWMOGI) and an Adaptive Delay Operation Period Filter (ADOPF) to precisely extract fundamental positive-sequence components for grid synchronization. The ANFIS controller serves as the primary regulator for the common DC-link voltage, generating the necessary control components while incorporating feed-forward terms from solar and wind power to enhance dynamic response and mitigate battery stress. A coordinated energy management strategy is implemented to optimize power sharing among the grid, renewable sources, and EV loads. The effectiveness of this approach is demonstrated through improved DC-link voltage regulation, enhanced renewable utilization, and superior grid current quality, ensuring the system remains compliant with power quality standards even under variable operating conditions.

I. Introduction

The increasing penetration of renewable energy sources (RESs), distributed energy resources (DERs), battery energy storage systems (BESSs), and electric vehicles (EVs) has accelerated the development of advanced microgrid architectures for modern power systems

[1]–[4]. Among these, dc microgrids have received considerable attention because photovoltaic (PV) systems, battery storage, EV batteries, and several modern electronic loads are inherently dc in nature [5], [6]. A common dc bus can reduce unnecessary power conversion stages, improve conversion efficiency, and facilitate the integration of renewable sources, energy storage, EVs, and dc loads [7], [8]. However, renewable intermittency and power-electronic loads introduce challenges in dc-link voltage regulation, power-flow coordination, battery management, and grid-side power quality [9]–[12]. PV and wind energy systems are strongly dependent on environmental conditions. PV output varies with solar irradiance and temperature, whereas wind generation depends mainly on wind speed [13], [14]. Consequently, renewable power at the dc bus can vary significantly, while EV charging and dc loads introduce additional changes in demand. The resulting power mismatch must be compensated by the BESS and utility grid to maintain the dc-link voltage at its reference value [15], [16]. Therefore, coordinated operation of renewable sources, battery storage, EVs, loads, and the utility grid is essential for reliable grid-interactive dc-microgrid operation. Several control strategies have been developed for dc microgrids. Droop control is widely used because of its simple decentralized implementation and power-sharing capability [3], [17]. However, conventional droop control can produce dc-bus voltage deviations and inaccurate power sharing because of line impedance, converter parameter variations, unequal converter ratings, and changing operating conditions [18]. Hierarchical control incorporating primary, secondary, and tertiary levels has been proposed to improve voltage regulation, power sharing, and energy management [3], [19]. Nevertheless, its performance can depend on controller tuning, communication requirements, and the characteristics of the connected distributed resources. Proportional-integral (PI) controllers are also extensively used for dc-link voltage and converter current regulation because of their simple structure and ease of implementation [20]. However, fixed-gain PI controllers may provide limited dynamic performance under renewable intermittency, EV charging variations, battery SOC changes, and load disturbances. The nonlinear behavior of power converters and the coupling among renewable sources, BESS, EVs, and the grid further motivate the use of advanced control techniques, including adaptive control, fuzzy logic, artificial neural networks (ANNs), model predictive control, and hybrid intelligent approaches [21], [22]. Among these techniques, the adaptive neuro-fuzzy inference system (ANFIS) combines the learning capability of neural networks with the reasoning capability of fuzzy inference systems [23]. It can establish nonlinear input-output relationships and provide adaptive control under varying operating conditions. ANFIS-based control and energy-management techniques have been investigated for renewable-energy systems, microgrids, distributed energy resources, and power converters [24], [25]. However, the coordinated use of ANFIS for dc-link voltage regulation with renewable power feed-forward compensation, battery energy management, EV power exchange, and grid-current control remains comparatively limited. The BESS plays an important role in mitigating renewable intermittency and maintaining the power balance of dc microgrids [26], [27]. It can absorb surplus renewable power and supply power during generation deficits. However, excessive battery charging and discharging can increase battery stress and affect its useful lifetime. Therefore, the battery operating mode should be determined according to renewable generation, load demand, EV requirements, grid power exchange, and SOC limits [28]. This coordinated energy management becomes particularly important when stationary BESS and EV batteries are connected to the same dc bus. EV charging introduces a significant and rapidly varying power demand into the dc microgrid [29]. Conversely, bidirectional EV chargers enable grid-to-vehicle (G2V) and vehicle-to-grid (V2G) operation, allowing EV batteries to participate in energy management and grid-support functions [30], [31]. Previous studies have demonstrated the potential of EVs for peak-load management, renewable-energy utilization, and grid support [32], [33]. However, coordinated operation of EVs with PV, wind, stationary BESS, dc loads, and utility-grid power exchange requires an integrated converter-control and energy-management strategy. The grid-interfaced converter is responsible for maintaining the dc-link voltage and controlling active-power exchange with the utility grid. It must also generate balanced and sinusoidal grid currents with low harmonic distortion. Accurate grid-voltage synchronization and fundamental positive-sequence

extraction are therefore essential. Distorted and unbalanced grid voltages can introduce errors in reference-current generation and degrade grid-side power quality [34]. Advanced filtering techniques have consequently been investigated for improving fundamental-component extraction. In particular, anti-windup mixed-order generalized integrator (AWMOGI) and adaptive delay operation period filter (ADOPF) techniques have been proposed for fundamental and positive-sequence extraction under distorted and unbalanced grid conditions [35]. However, their coordinated integration with intelligent dc-link control, battery energy management, renewable feed-forward compensation, and EV charging in a dc microgrid remains an area requiring further investigation. From the above discussion, existing studies have mainly addressed individual aspects such as dc-microgrid voltage regulation, renewable-energy management, BESS control, EV charging, intelligent control, or grid synchronization. A unified framework simultaneously considering renewable intermittency, dc-link voltage regulation, battery SOC constraints, EV charging demand, renewable feed-forward compensation, grid synchronization, and grid-current control remains comparatively limited. In particular, the coordinated interaction between ANFIS-based dc-link regulation and adaptive battery energy management under simultaneous PV, wind, EV, and load variations requires further investigation. To address these limitations, this paper proposes an ANFIS-based dc-link voltage regulation and energy-management strategy for a grid-interactive PV–wind–battery EV integrated dc microgrid. The proposed system integrates PV and wind sources through dc-dc boost converters, a BESS through a bidirectional dc-dc converter, and an EV charging/discharging unit through a bidirectional power-electronic interface. The grid-interfaced converter regulates the common dc-link voltage and controls power exchange with the utility grid. The ANFIS controller generates the dc-link control component according to the voltage error and its variation, while PV and wind power feed-forward components provide anticipatory compensation for renewable-power fluctuations and reduce unnecessary battery intervention. An adaptive battery energy-management strategy coordinates battery charging, discharging, and standby modes according to instantaneous power balance and SOC limits. EV charging/discharging is coordinated with renewable availability, battery condition, dc-load demand, and grid power exchange. For grid-side control, AWMOGI-based filtering and ADOPF-based positive-sequence extraction are employed to obtain accurate fundamental grid-voltage components under distorted and unbalanced conditions. The resulting reference currents are tracked using a hysteresis current controller to generate the switching signals of the grid-interfaced converter.

The main contributions of this paper are summarized as follows:

1. An integrated PV–wind–BESS–EV grid-interactive dc microgrid is developed to coordinate renewable generation, battery storage, EV charging/discharging, dc loads, and utility-grid power exchange.
2. An ANFIS-based dc-link voltage controller is developed to provide adaptive nonlinear voltage regulation under renewable-generation and load variations.
3. An adaptive battery energy-management strategy is proposed to determine battery charging, discharging, and standby operation based on instantaneous power balance and SOC constraints.
4. PV and wind power feed-forward compensation is incorporated into the dc-link control structure to improve transient response and reduce unnecessary battery power fluctuations.
5. An AWMOGI–ADOPF-based grid synchronization and positive-sequence extraction technique is incorporated to improve reference-current generation under distorted and unbalanced grid-voltage conditions.
6. A hysteresis current controller is employed for accurate tracking of the reference grid currents and generation of the switching signals for the grid-interfaced converter.
7. The effectiveness of the proposed coordinated strategy is evaluated under renewable-generation intermittency, load variations, battery charging/discharging, EV charging demand, and grid power exchange, demonstrating its capability to maintain stable dc-link operation and improve overall grid-interactive microgrid performance.

II. System Configuration

The system configuration of the proposed method features a grid-interactive dc microgrid that integrates photovoltaic (PV) and wind energy systems through dc-dc boost conversion stages to a common dc-link bus as shown in Fig.1. This architecture includes a battery energy storage system (BESS) and an electric vehicle (EV) charging system, both of which are interfaced at the dc bus side via bidirectional dc-dc converters to enable controlled charging, discharging, and vehicle-to-grid (V2G) power exchange. A grid-interfaced converter (GIC) acts as the primary link to the utility grid, regulating the common dc-link voltage and controlling the bidirectional power flow. The control framework utilizes an adaptive neuro-fuzzy inference system (ANFIS) to generate voltage regulation components, further enhanced by PV and wind power feed-forward terms to optimize dynamic response and mitigate battery stress. To maintain high power quality and reliable synchronization under distorted grid conditions, the system incorporates an anti-windup mixed-order generalized integrator (AWMOGI) filter and an adaptive delay operation period filter (ADOPF) for precise fundamental positive-sequence extraction, while a hysteresis current controller regulates the grid currents.

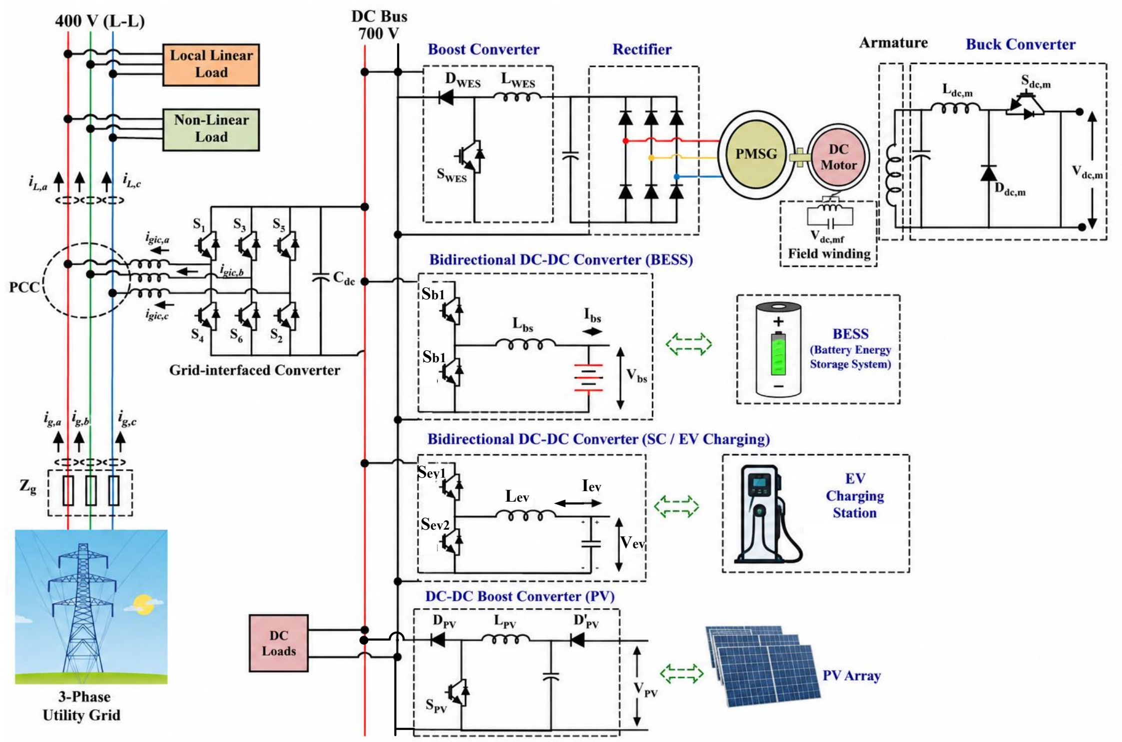

Fig. 1. Proposed grid-connected renewable energy system with PV, wind, BESS, and EV charging integration.

III. Solar PV Configuration

The solar photovoltaic (PV) system is used as the primary renewable energy source in the proposed hybrid energy storage system. The PV array converts incident solar irradiance into electrical power and supplies the common dc bus through a dc–dc boost converter as shown in Fig.2. The PV power varies with solar irradiance and cell temperature; therefore, an MPPT controller is employed to extract the available maximum power. PV systems commonly use a dc–dc converter as the interface between the PV source and the dc bus.

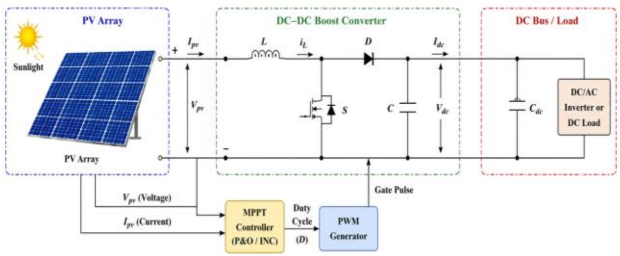

Fig. 2. Solar PV configuration with MPPT-controlled DC–DC boost converter and DC-bus interface.

1) PV Cell Mathematical Model

The single-diode equivalent circuit is considered for modeling the PV cell. The output current is expressed as

$$I_{p_v} = I_{Ph} - I_0\left[exp\left(\frac{V_{pv}+I_{pv}R_S}{nN_SV_T}\right)-1\right] - \frac{v_{pv}+I_{pv}R_S}{R_{sh}} \quad (1)$$

where Iph is the photocurrent, I0 is the reverse saturation current, Rs and Rsh are the series and shunt resistances, n is the diode ideality factor, and Ns is the number of series-connected cells.

The thermal voltage is given by

$$V_T = \frac{kT_c}{q} \tag{2}$$

where k is the Boltzmann constant, Tc is the cell temperature, and q is the electronic charge.

The photocurrent is approximately related to solar irradiance by

$$I_{Ph} = \left[I_{Ph,ref} + k_I\left(T_c - T_{ref}\right)\right]\frac{G}{G_{ref}} \tag{3}$$

where G is the incident solar irradiance and G_{ref} is the reference irradiance.

The saturation current can be expressed as

$$I_0 = I_0,ref\left(\frac{T_c}{T_{ref}}\right)^3 exp\left[\frac{qE_g}{nk}\left(\frac{1}{T_{ref}} - \frac{1}{T_c}\right)\right] \tag{4}$$

3) DC–DC Boost Converter

A boost converter is connected between the PV array and the dc-link to increase the PV voltage to the required dc-bus level. During continuous-conduction operation, the ideal voltage conversion ratio is

$$V_{dc=}\frac{V_{Pv}}{1-D_{pv}} \tag{5}$$

where Dpv is the boost-converter duty ratio.

Hence,

$$D_{Pv} = 1 - \frac{V_{Pv}}{V_{dC}} \tag{6}$$

The inductor voltage during the ON state is

$$V_{L,on} = V_{PV}, \tag{7}$$

whereas during the OFF state,

$$V_{L,0ff} = V_{Pv} - V_{dc}. \tag{8}$$

Applying the volt-second balance,

$$D_{Pv}V_{pv} + (1 - D_{Pv})(V_{Pv} - V_{dc}) = 0, \tag{9}$$

which gives the boost-converter voltage relationship in (9).

4) MPPT Control

The maximum power point is obtained from

$$\frac{dP_{Pv}}{dV_{Pv}} = 0 \tag{10}$$

and, since

$$P_{Pv} = V_{pv}I_{pv}, \tag{11}$$

the maximum-power condition becomes

$$I_{Pv} + V_{Pv}\frac{dI_{Pv}}{dV_{pv}} = 0 \tag{12}$$

Thus,

$$\frac{dI_{Pv}}{dV_{Pv}} = -\frac{I_{pv}}{V_{pv}} \tag{13}$$

at the maximum power point.

For an incremental-conductance MPPT algorithm, the condition is therefore

$$\frac{\Delta I_{Pv}}{\Delta V_{Pv}} = -\frac{I_{Pv}}{V_{pv}} \tag{14}$$

The MPPT controller generates the reference voltage or duty ratio required to force the PV operating point toward the maximum power point.

5) Overall Solar-PV Power Flow

The complete solar-energy conversion path can be represented as

$$G, T_c \rightarrow PVArray \rightarrow MPPT \rightarrow Boost\ Converter \rightarrow DC\ Bus$$

The PV system consequently supplies the available renewable power to the dc bus, while the battery and supercapacitor compensate for variations between PV generation and load/grid power demand. This type of coordinated PV and energy-storage interface is also used in grid-connected renewable-energy systems to manage power flow between the PV source, storage, and dc bus.

IV. EV Battery Charging and Discharging

The EV battery is connected to the common dc bus through a bidirectional DC–DC converter. The converter enables buck-mode operation during battery charging and boost-mode operation during battery discharging as shown in Fig.3. This bidirectional power flow allows the EV battery to absorb surplus renewable power and return stored energy to the dc bus when additional power is required.

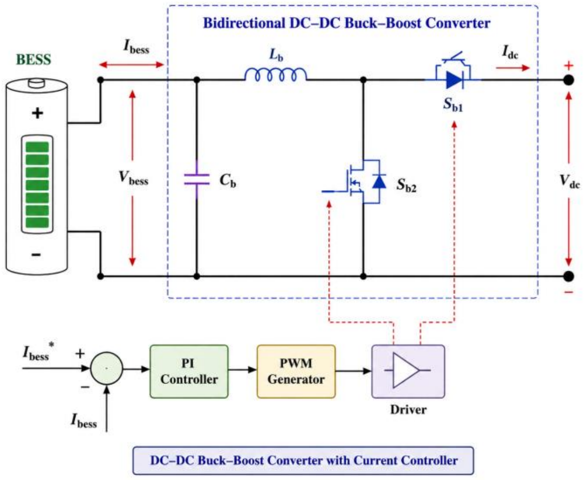

Fig. 3. Bidirectional EV battery charging and discharging system using a DC–DC converter.

1) Battery Charging Mode

During charging, the bidirectional converter operates in buck mode. The dc-bus voltage is stepped down to the battery voltage, and the charging current is controlled according to the battery-current reference.

For an ideal buck converter,

$$V_{bat} = D_b V_{dc} \quad (15)$$

where V_{bat} is the battery voltage, V_{dc} is the dc-link voltage, and D_b is the converter duty ratio.

Therefore,

$$D_b = \frac{V_{bat}}{V_{dc}} \quad (16)$$

The battery charging power is

$$P_{ch} = V_{bat} I_{ch} \quad (17)$$

where Ich is the battery charging current.

Considering converter efficiency,

$$P_{bat} = \eta_{dc-dc} P_{dc} \quad (18)$$

where η_{dc-dc} is the bidirectional converter efficiency.

The battery state of charge (SOC) during charging can be represented by

$$SOC(t) = SOC(t_0) + \frac{\eta_{ch}}{Q_{bat}} \int_{t_0}^{t} I_{ch}(\tau)\, d\tau \quad (19)$$

where Qbat is the battery capacity and ηch is the charging efficiency.

2) Battery Discharging Mode

During discharging, the converter operates in **boost mode**, transferring energy from the EV battery to the dc bus. The ideal boost-converter relationship is

$$V_{dc} = \frac{V_{bat}}{1-D_b}. \quad (20)$$

Hence, the required duty ratio is

$$D_b = 1 - \frac{v_{bat}}{V_{dc}} \quad (21)$$

The battery discharging power is

$$P_{dis} = V_{bat} I_{dis} \quad (22)$$

and the dc-bus power supplied by the battery is approximately

$$P_{dc} = \eta_{dc-dc} P_{dis} \quad (23)$$

During discharge, the SOC decreases according to

$$SOC(t) = SOC(t_0) - \frac{1}{\eta_{dis} Q_{bat}} \int_{t_0}^{t_I} di\, S^{(\tau)\, d\tau} \quad (24)$$

3) Battery Power Balance

The battery power can be represented as

$$P_{bat} = V_{bat} I_{bat} \quad (25)$$

The sign convention can be defined as

$P_{bat} > 0$ *charging*

And

$P_{bat} < 0$ *discharging*

The overall dc-bus power balance is

$$P_{PV} + P_{grid} + P_{bat} = P_{EV} + P_{load} + P_{loss} \quad (26)$$

where PEV represents the EV charging demand.

4) Battery Current Control

The charging/discharging current is regulated using the reference current I_{bat}^*. The current error is

$$e_i = I_{bat}^* - I_{bat} \cdot \quad (27)$$

For a PI-based current controller,

$$u_{PI} = K_P e_i + K_i \int e_i\, d_t \quad (28)$$

or in the Laplace domain,

$$G_{PI}(s) = K_p + \frac{K_i}{s} \quad (29)$$

The controller output generates the required PWM duty ratio for the bidirectional DC–DC converter.

5) Charging and Discharging Operation

The operating modes can be summarized as

$P_{surplus} > 0 \Rightarrow EV\ Battery\ Ch\,arg\,ing$

And

$P_{deficit} > 0 \Rightarrow EV\ Battery\ Discharging$

Thus, during periods of surplus PV power, the EV battery is charged through buck operation. During periods of insufficient PV power, the battery operates in boost mode and supplies power to the dc bus or grid.

V. Wind Energy Conversion System Configuration

The wind energy conversion system (WECS) is integrated with the common DC bus through a permanent-magnet synchronous generator (PMSG) and a power-electronic conversion stage. The wind turbine converts the kinetic energy of the wind into mechanical power, which is then converted into electrical power by the PMSG as shown in Fig.4. A rectifier and DC–DC converter regulate the generated power before supplying the DC bus.

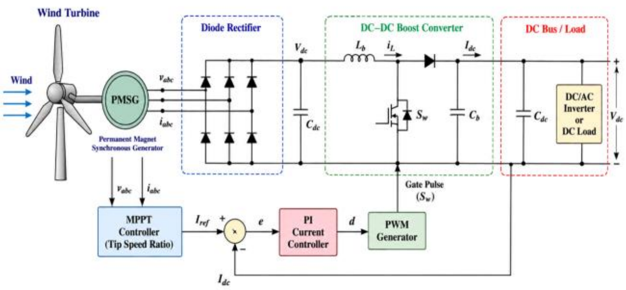

Fig. 4. Configuration of the PMSG-based wind energy conversion system with rectifier and DC–DC converter

1) Wind Turbine Power

The mechanical power extracted from the wind is expressed as

$$P_w = \frac{1}{2} \rho_{A v_w^3} C_P(\lambda, \beta) \quad (30)$$

Where ϱ is the air density, A is the swept area, V_ω is the wind speed, Cp is the power coefficient, λ is the tip-speed ratio, and β is the blade pitch angle.

The swept area of the turbine is

$$A = \pi R^2 \quad (31)$$

where R is the turbine blade radius.

The tip-speed ratio is defined as

$$\lambda = \frac{\omega_m R}{V_\omega} \quad (32)$$

where ω_m is the mechanical angular speed of the turbine. The turbine torque is obtained from

$$T_w = \frac{P_w}{\omega_m} \quad (33)$$

2) Power Coefficient

The aerodynamic efficiency of the wind turbine is represented by C_p, which is a function of λ and β:

$$C_p = C_p(\lambda, \beta) \quad (34)$$

For maximum power extraction, the turbine is operated close to the optimum tip-speed ratio λ_{opt}. Therefore,

$$\lambda = \lambda_{opt} \quad (35)$$

and the corresponding maximum power coefficient is

$$C_{P,max} = C_P(\lambda_{oPt}, \beta) \quad (36)$$

3) PMSG Model

The electrical dynamics of the PMSG in the dq reference frame can be expressed as

$$V_d = R_s I_d + L_d \frac{dI_d}{dt} - \omega_e L_q I_q \quad (37)$$

$$V_q = R_s I_q + L_q \frac{dI_q}{dt} + \omega_e (L_d I_d + \psi f) \quad (38)$$

where Rs is the stator resistance, Ld and Lq are the d- and q-axis inductances, ωe is the electrical angular speed, and ψf is the permanent-magnet flux linkage.

The electromagnetic torque is

$$T_e = \frac{3}{2} p [\psi_f I_q + (L_d - L_q) I_d I_q] \quad (39)$$

For a surface-mounted PMSG, where Ld≈Lq,

$$T_e = \frac{3}{2} p \psi_f I_q \quad (40)$$

where p is the number of pole pairs.

The mechanical dynamics are given by

$$J \frac{d\omega_m}{dt} = T_w - Te - B\omega_m \quad (41)$$

where J is the combined rotational inertia and B is the mechanical damping coefficient.

4) Wind Energy Conversion and DC-Link Interface

The generated three-phase electrical power from the PMSG is converted into DC power through a rectifier:

$$P_{dc} = V_{dc} I_{dc} \quad (42)$$

Considering converter losses,

$$P_{dc} = \eta_{rec} P_{PMSG} \quad (43)$$

Where η_{rec} is the rectifier efficiency.

The DC–DC converter subsequently regulates the generated power delivered to the common DC bus. The overall wind power path is therefore

$$V_w \rightarrow wind\ Turbine \rightarrow PMSG \rightarrow Rectifier \rightarrow DC - DC\ Converter \rightarrow DCBus$$

5) Maximum Power Extraction

For maximum wind-energy extraction, the turbine speed is controlled according to the wind velocity such that

$$\omega_{m,opt} = \frac{\lambda_{opt} v_w}{R} \quad (44)$$

The corresponding maximum turbine power is

$$P_{w,max} = \frac{1}{2} \rho A v_w^3 C_{p,max} \quad (45)$$

Thus, the controller adjusts the generator operating point to maintain the optimum tip-speed ratio and extract maximum available wind power.

VI. Proposed Control Strategy

The proposed control scheme integrates the grid interfaced VSC with AWMOGI filtering, ADOPF positive sequence extraction, abc-dq transformation, ANFIS based DC link regulation, battery mode selection, and PV/wind feed forward compensation. The filtered grid voltages are synchronized and transformed into the dq frame, while the ANFIS controller regulates the DC link voltage as shown in Fig. 5. The battery controller manages charging and discharging according to the load demand and SOC, whereas PV and wind feed forward terms improve the response to renewable power variations. The resulting reference grid currents are transformed back to the abc frame and compared with the actual grid currents. The hysteresis current controller generates the switching pulses S1–S6 for the grid interfaced VSC, thereby ensuring accurate current tracking, controlled power exchange, and stable DC bus operation.

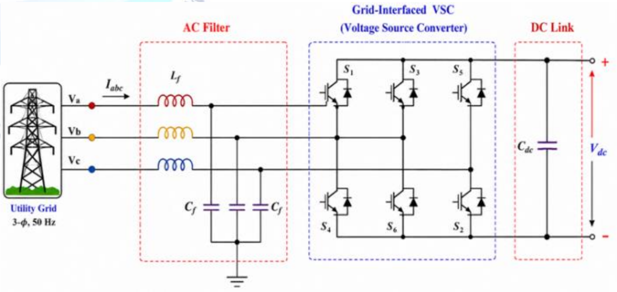

Fig. 5. Grid-interfaced voltage source converter

The proposed control strategy integrates AWMOGI, ADOPF, ANFIS, battery energy management, feed-forward compensation, and hysteresis current control for effective grid-connected operation. The AWMOGI and ADOPF blocks extract the fundamental and positive-sequence components of the grid voltage for accurate synchronization. The ANFIS controller regulates the dc-link voltage and generates the required active-current reference as shown in Fig.6. The battery management block determines charging or discharging operation according to the power demand and SOC. PV and wind power feed-forward components improve the dynamic response, while the hysteresis current controller generates the converter switching pulses. Thus, the proposed controller provides stable dc-link regulation, coordinated power management, and accurate grid-current tracking under varying operating conditions.

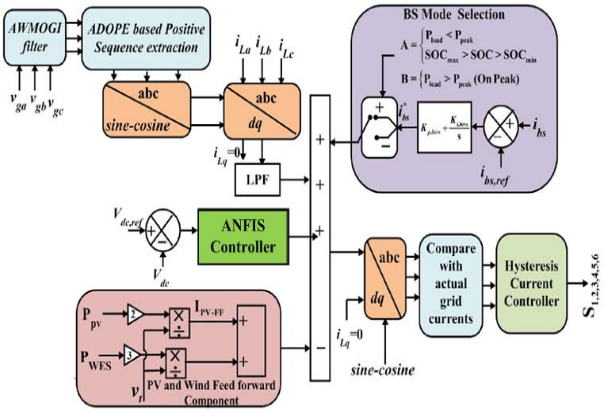

Fig.6. Proposed ANFIS-based control strategy for renewable energy integrated grid-connected system.

A. Anti-Windup Mixed-Order Generalized Integrator

The anti-windup mixed-order generalized integrator (AWMOGI) is employed to extract the fundamental component of the distorted utility-grid voltage while reducing dc offset and steady-state oscillations. The AWMOGI structure incorporates an anti-windup gain β, resonant frequency ω_o , and gain parameter m. According to the proposed controller, the closed-loop transfer functions of the AWMOGI are given by

$$H_1(s) = \frac{v_1(s)}{V_g(S)} = \frac{m\omega_o s + m\omega_o\beta}{s^2 + s(2\beta + m\omega_o) + (\omega_0^2 + \beta^2 + \beta m\omega_o)} \quad (46)$$

And

$$H_2(5) = \frac{v_2(5)}{V_{g(s)}} = \frac{m\omega_0^2}{s^2 + s(2\beta + m\omega_o) + (\omega_0^2 + \beta^2 + \beta m\omega_o)} \quad (47)$$

To further suppress the dc component, an additional branch is introduced. Its transfer function is

$$H_3(s) = \frac{v_3(s)}{v(s)} = \frac{mm\omega_0^2 + m\omega_0^3}{s^3 + As^v + Bs + C} \quad (48)$$

Where

$$A = \beta + m\omega_0 + \omega_0 \quad (49)$$

$$B = \omega_0^2 + m\omega_0^2 + \beta m\omega_0 \quad (50)$$

$$C = m\omega_0^2 + \omega_0^3 \quad (51)$$

The steady-state outputs at ωo=ωs are expressed as

$$v_1^{\infty}(t) = V_n\, sin(\omega_s t + \phi_s) \quad (52)$$

$$v_2^{\infty}(t) = V_{dc} - V_n\, cos(\omega_s t + \phi_s) \quad (53)$$

$$v_3^{\infty}(t) = mV_{dc} \quad (54)$$

Hence, the AWMOGI output components are

$$E_{AWMOGI} = v_1$$

$$F_{AWMOGI} = v_2 - v_3$$

The parameter m provides a tradeoff between transient response and filtering capability; the source reports an optimized value of m=1.52.

B. Hierarchical-Loop Controller

The hierarchical-loop controller consists of outer and inner control loops. The outer loop employs a fractional-order proportional-tilt-integral-derivative (FPTID) controller, whereas the inner loop uses a fractional-order proportional-derivative controller with filtering (FPDN). This two-loop arrangement improves dc-link-voltage regulation and transient stability compared with a single-loop structure.

The outer-loop controller is represented by

$$H_{FPDN}(s) = k_{P1} + k_{d1}\frac{M}{1 + M\frac{1}{s^{\eta}}} \quad (55)$$

where kp1 and kd1 are proportional and derivative gains, M is the filter parameter, and γ1 represents the fractional-order parameter.

The inner-loop controller is expressed as

$$H_{FPTID}(s) = k_{P^2} + \frac{k_t}{s^n} + \frac{k_{i2}}{s^{\mu 2}} + k_{d2}s^{\gamma 2} \quad (56)$$

where kp2, kt, ki2, and kd2 denote the proportional, tilt, integral, and derivative gains, respectively, while n, μ2, and γ2 are the corresponding fractional orders. The hierarchical structure therefore provides fast inner-loop regulation together with slower outer-loop dc-link-voltage regulation, allowing the converter to maintain stable operation during renewable-power and load variations.

VII. PROPOSED ANFIS CONTROLLER DESIGN

The proposed adaptive neuro-fuzzy inference system (ANFIS) controller is employed to regulate the dc-link voltage and improve the dynamic response of the grid-interfaced converter. Unlike a conventional PI controller, the ANFIS controller combines the learning capability of an artificial neural network with the rule-based decision-making property of fuzzy logic. The controller continuously processes the dc-link voltage error and its rate of change to generate the appropriate control signal for the converter. The uploaded reference paper uses hierarchical control for dc-link regulation, but it does not provide an ANFIS formulation; therefore, the following ANFIS structure is a proposed controller formulation for your system as shown in Fig.7.

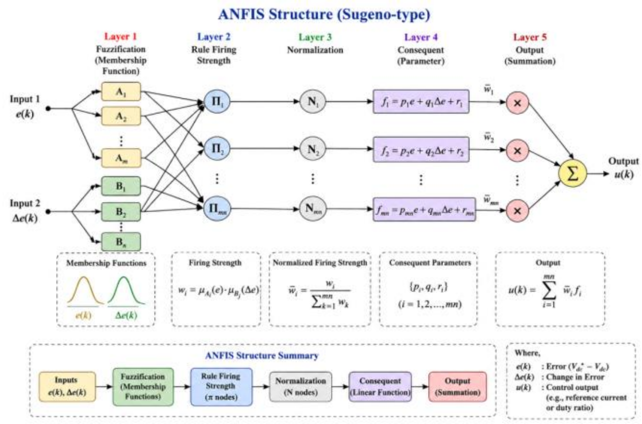

Fig. 7. Structure of the proposed ANFIS controller.

A. ANFIS Input Variables

The dc-link voltage error is defined as

$$e(k) = V_{dc}^{*}(k) - V_{dc}(k) \quad (57)$$

where V_{dc}^{*} is the reference dc-link voltage and V_{dc} is the measured dc-link voltage.

The change in error is calculated as

as its two input variables. The controller output is defined as

$$u_{ANFIS} = \Delta D$$

where ΔD represents the required change in converter duty ratio. The updated duty ratio is

$$D(k) = D(k-1) + \Delta D(k). \quad (58)$$

This formulation allows the controller to increase or decrease the converter duty ratio according to the instantaneous dc-link voltage deviation.

B. ANFIS Membership Functions

For a first-order Sugeno ANFIS structure, each input is divided into five linguistic variables:

$$\{NB, NS, ZE, PS, PB\}$$

where NB, NS, ZE, PS, and PB denote negative-big, negative-small, zero, positive-small, and positive-big, respectively.

A Gaussian membership function can be expressed as

$$\mu_{Ai(x)} = exp\left[-\frac{(x-c_i)^2}{2\sigma_i^2}\right] \quad (59)$$

where ci is the center and σi is the width of the membership function.

C. ANFIS Rule Base

The fuzzy rules are expressed in the form

R_i: IF e is A_i AND Δe is B_i THEN $f_i = p_i e + q_i \Delta_e + r_i$

For two inputs with five membership functions each, a total of

$$N_R = 5 \times 5 = 25$$

fuzzy rules are generated.

The firing strength of the ith rule is

$$w_i = \mu_{A_i}(e)\mu_{B_i}(\Delta e) \quad (60)$$

The normalized firing strength is

$$\bar{w}_i = \frac{w_i}{\sum_{J=1}^{N_R} \omega_j} \quad (61)$$

D. ANFIS Output Computation

The consequent output of each rule is

$$f_i = p_i e + q_i \Delta e + r_i \cdot \quad (62)$$

The final ANFIS output is obtained through weighted averaging:

$$u_{ANFIS} \frac{\sum_{i=1}^{N_R} w_i(p_i e + q_i \Delta e + r_i)}{\sum_{i=1}^{N_R} w_1} \quad (63)$$

The obtained control signal is then converted into the PWM duty ratio according to (63).

E. ANFIS Training

The ANFIS parameters are trained using input-output data obtained from the converter under different operating conditions. The training objective is to minimize the voltage-tracking error. The mean-square error (MSE) can be defined as

$$J = \frac{1}{N}\sum_{k=1}^{N}[V_{dc}^{*}(k) - V_{dc}(k)]^2 \quad (64)$$

The ANFIS parameters are adjusted iteratively to minimize J. The trained controller subsequently provides the appropriate duty-ratio command without requiring manually retuned PI gains for every operating condition.

VIII. Simulation results and Discussion

A. PV System Performance under Varying Operating Conditions

Fig. 8 presents the PV voltage, current, and power responses over a 1 s simulation period under varying operating conditions. The PV voltage Vpv rapidly reaches approximately 300 V at the beginning of the simulation and remains nearly constant from 0 to 1 s. The PV current Ipv initially reaches about 65 A and changes to approximately 53 A at 0.2 s, 34 A at 0.3 s, and 20 A at 0.4 s, remaining stable thereafter. Correspondingly, the PV power Ppv decreases from approximately 20 kW initially to 16 kW at 0.2 s, 10 kW at 0.3 s, and 6 kW at 0.4 s. The stable voltage and smooth current and power transitions demonstrate effective PV operation under varying conditions.

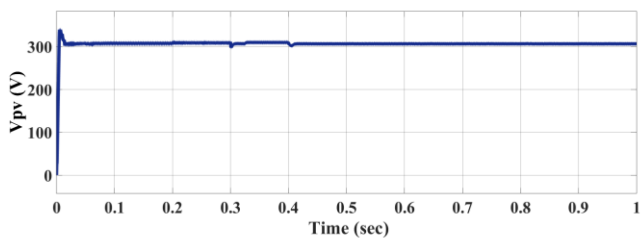

(a)

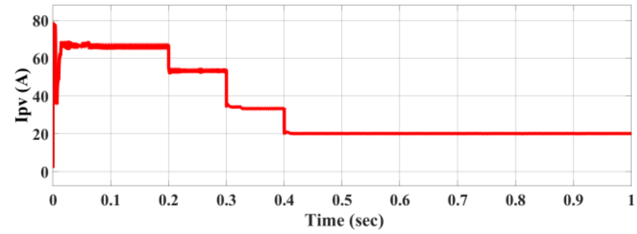

(b)

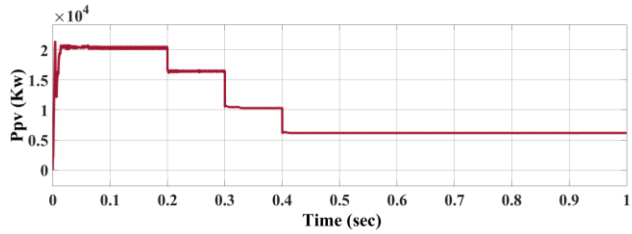

(c)

Fig. 8. Simulation results of (a) PV voltage Vpv, (b) PV current Ipv, and (c) PV power Ppv under varying operating conditions.

B. Wind Energy System Performance Under Varying Operating Conditions

Fig. 9 presents the wind turbine current Iwind and generated power Pwind over a 1 s simulation period. The wind current exhibits an initial transient and then remains within approximately ±60 A up to 0.5 s. It subsequently decreases in magnitude at 0.6 s, 0.7 s, and 0.75 s, indicating changes in wind operating conditions. Correspondingly, the wind power initially reaches approximately 24 kW, decreases to about 20 kW at 0.5 s, 14 kW at 0.62 s, and approximately 6 kW after 0.73 s. The response demonstrates stable wind power extraction and smooth adaptation to changing operating conditions.

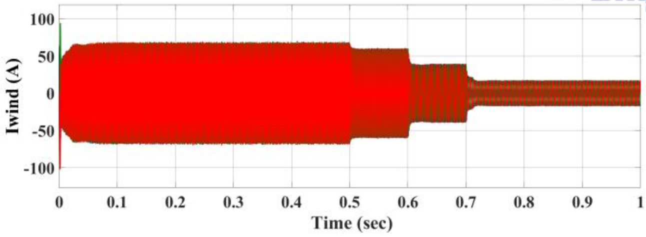

(a)

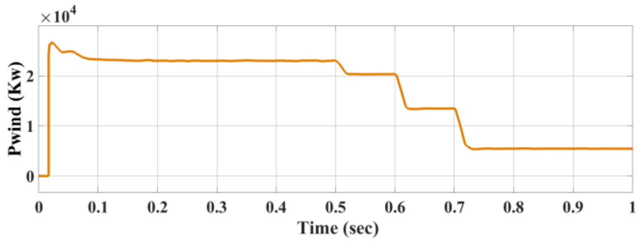

(b)

Fig. 9. Simulation results of (a) Wind Turbine Current Iwind and (b) Wind Turbine Generated Power Pwind under varying wind conditions.

C. Battery Energy Storage System Performance

Fig. 10 presents the battery voltage, current, power, and SOC responses over a 1 s simulation period. The battery voltage Vbat quickly stabilizes at approximately 325 V and remains nearly constant throughout the simulation. The battery current Ibat exhibits an initial transient, reaching approximately 35 A, and subsequently settles around 25–30 A with small variations. Correspondingly, the battery power Pbat initially rises to approximately 10 kW and then remains within approximately 7–10 kW. The battery SOC shows a gradual decrease from approximately 63.81% to 63.807%, indicating controlled battery energy utilization. Overall, the responses demonstrate stable battery operation and effective power support under varying operating conditions.

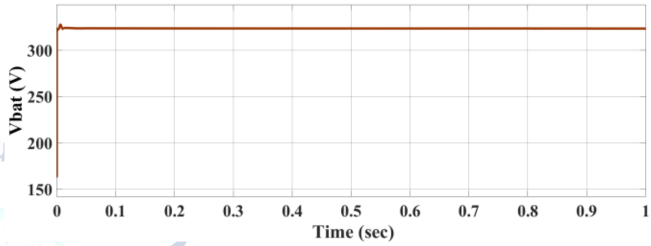

(a)

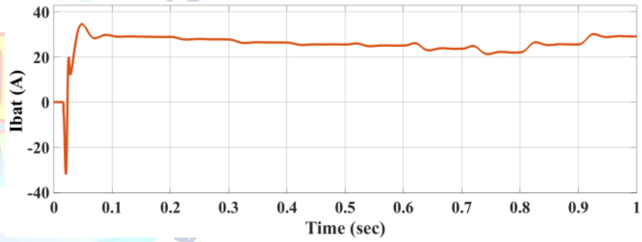

(b)

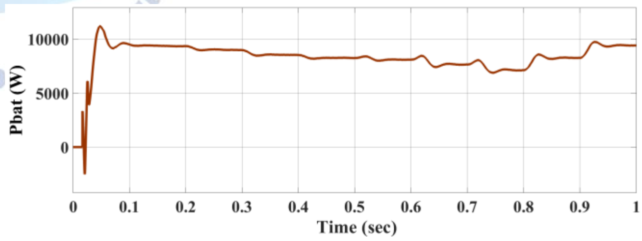

(c)

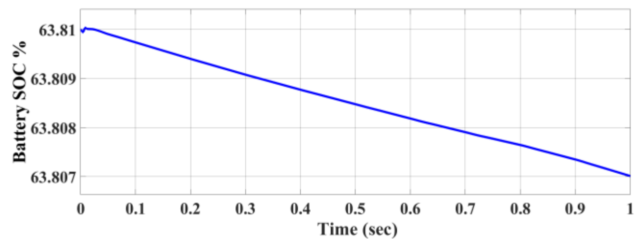

(d)

Fig. 10. Simulation results of (a) Battery Voltage Vbat, (b) Battery Current Ibat, (c) Battery Power Pbat, and (d) Battery State of Charge (SOC) under varying operating conditions.

D. EV Battery Charging Performance

Fig. 11 presents the EV battery voltage, current, power, and SOC responses over a 1 s simulation period. The EV battery voltage Vev remains nearly constant at approximately 320 V throughout the simulation. The EV current Iev is close to zero during 0–0.8 s, followed by charging current levels of approximately −25 A from 0.8–0.9 s and −50 A from 0.9–1 s. Accordingly, the EV battery power Pev changes from near zero to approximately −8 kW and −16 kW, respectively, indicating increased charging power. The EV SOC remains nearly constant initially and increases slightly after 0.8 s, reaching approximately 79.3205% at 1 s. These responses demonstrate controlled EV battery charging with stable terminal voltage and SOC variation.

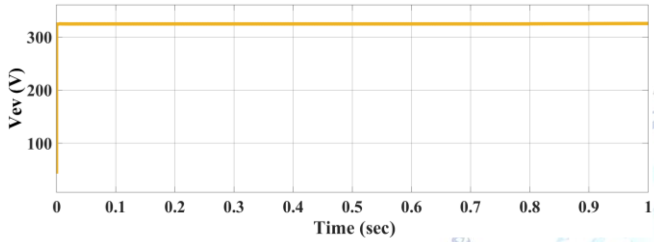

(a)

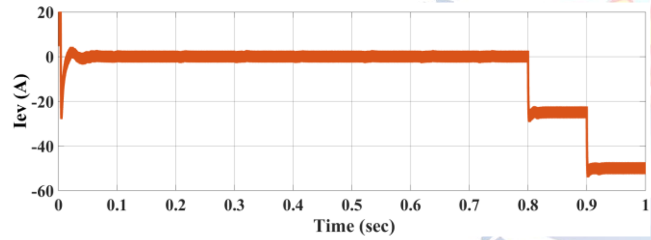

(b)

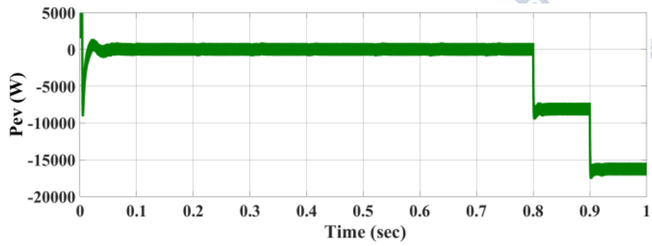

(c)

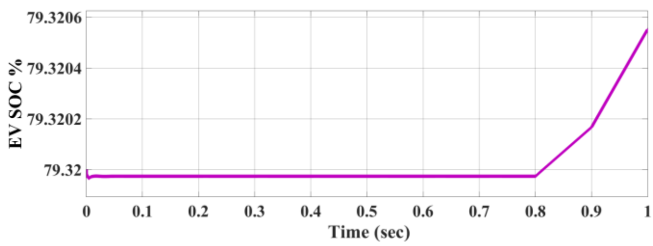

(d)

Fig. 11. Simulation results of (a) EV Battery Voltage VEV, (b) EV Battery Current IEV, (c) EV Battery Power PEV, and (d) EV Battery State of Charge (SOC) under charging conditions.

E. Grid-Connected System Performance

Fig. 12 presents the grid voltage Vabc, grid current Iabc, nonlinear load current INL, linear load current IL, grid power Pg, load power PL, DC-link voltage Vdc, and AC–DC converter power PAC−DC over a 1 s simulation period. The grid voltage remains balanced with a peak value of approximately ±330 V. The grid current initially reaches approximately ±100 A and decreases to about ±70 A at 0.1–0.2 s, ±50 A at 0.3–0.5 s, and ±30 A at 0.6 s. It approaches nearly zero around 0.75–0.8 s before increasing to approximately ±25–30 A at 1 s. The nonlinear load current remains periodic with a peak of approximately ±22 A, while the linear load current remains nearly sinusoidal at approximately ±10 A. The grid power changes from approximately −55 kW at 0 s to −35 kW at 0.1 s, −25 kW at 0.3 s, and nearly 0 kW at 0.7–0.8 s, followed by positive power flow near 1 s. The load power follows the corresponding power demand. The DC-link voltage Vdc rises rapidly during the initial transient and settles at approximately 800 V by 0.05 s, remaining regulated around 800 V from 0.05 to 1 s with only a small transient deviation. The AC–DC converter power increases to approximately 17.5 kW at 0.02 s and remains nearly constant thereafter. These results confirm effective DC-link voltage regulation, controlled grid-current tracking, and coordinated power exchange under varying operating conditions.

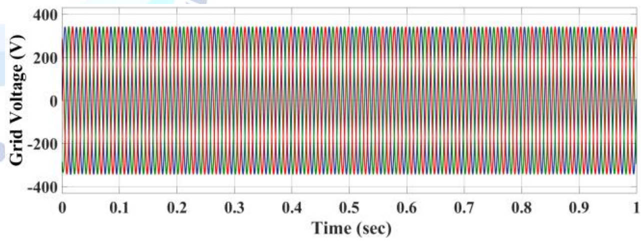

(a)

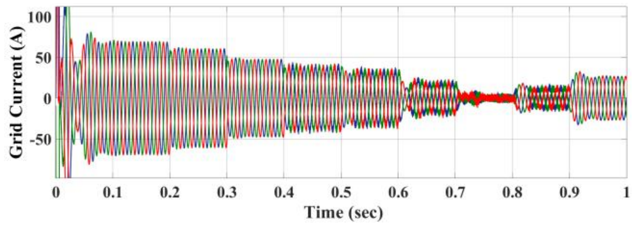

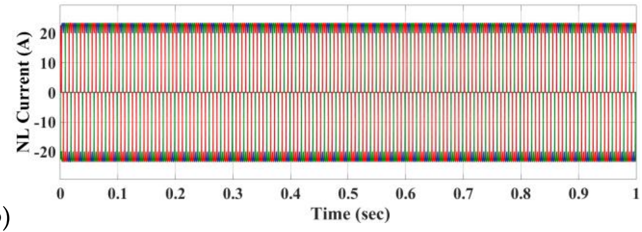

(b)

(c)

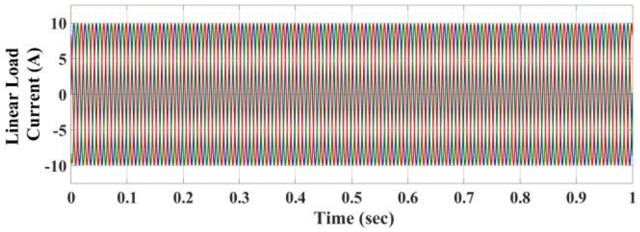

(d)

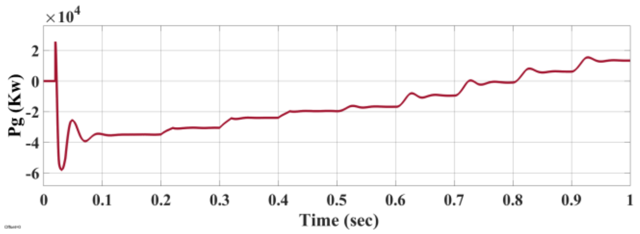

(e)

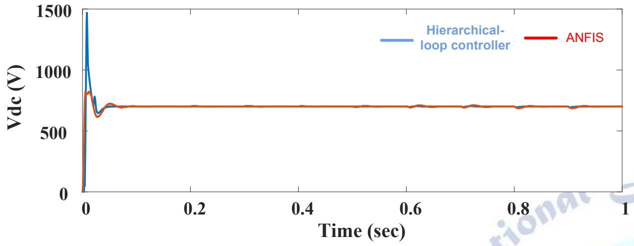

(f)

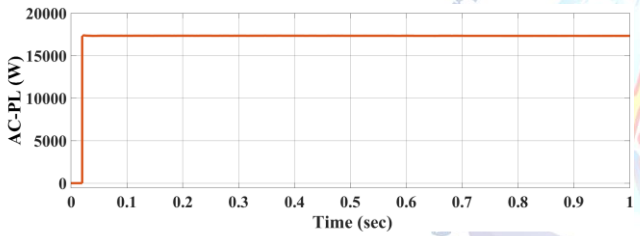

(g)

Fig.12 Simulation Results of (a) Grid Voltage Vabc, (b) Grid Current Iabc, (c) Nonlinear Load Current INL, (d) Linear Load Current IL, (e) Grid Power Pg, (f) Vdc, and (g) Load Power PL .

F. Grid Current THD Comparison

The first waveform represents the grid current with the Hierarchical-Loop Controller, giving a THD of 4.10%. The second waveform represents the grid current with the proposed ANFIS Controller, giving a significantly reduced THD of 1.18%. Thus, the proposed ANFIS controller improves the grid current quality by reducing THD from 4.10% to 1.18%, demonstrating better harmonic suppression and improved grid-side power quality as shown in Fig.13.

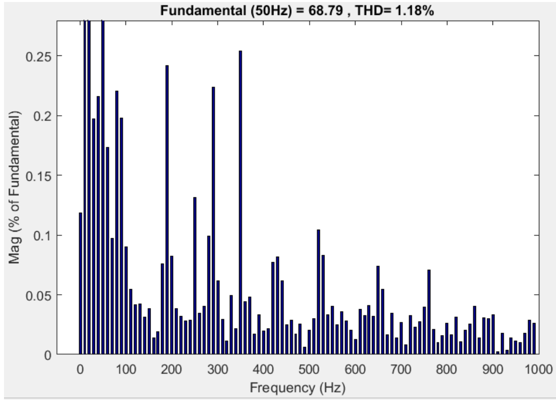

(a)

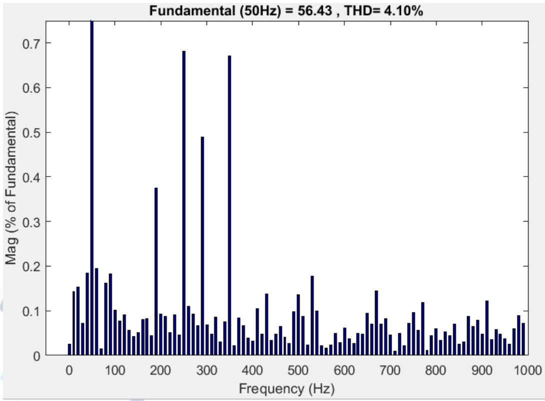

(b)

Fig.13 (a) Grid Current THD with Hierarchical-Loop Controller (b) Grid Current THD with Proposed ANFIS Controller

IX. Conclusion

The proposed hybrid renewable energy system with solar PV, wind energy, BESS, and EV battery charging demonstrates stable and coordinated operation under varying operating conditions. The PV and wind sources effectively supply renewable power, while the BESS supports power balancing and the EV battery operates with controlled charging. The grid interfaced VSC maintains stable voltage and current exchange with the utility grid, while the proposed ANFIS controller provides improved control performance and harmonic suppression compared with the hierarchical loop controller. The reduction in grid current THD from 4.10% to 1.18% confirms the effectiveness of the proposed control strategy in enhancing grid side power quality. Overall, the simulation results demonstrate that the proposed system provides effective renewable energy utilization, stable DC bus operation, coordinated energy management, controlled EV charging, and improved grid power quality, making it suitable for renewable integrated EV charging applications.

Conflict of interest statement

Authors declare that they do not have any conflict of interest.

REFERENCES

[1] H. Farzin, M. Fotuhi-Firuzabad, and M. Moeini-Aghtaie, "Role of outage management strategy in reliability performance of multimicrogrid distribution systems," IEEE Trans. Power Syst., vol. 33, no. 3, pp. 2359–2369, May 2018.

[2] M. Nabatirad, R. Razzaghi, and B. Bahrani, "Autonomous power balance in hybrid AC/DC microgrids," Int. J. Elect. Power Energy Syst., vol. 146, pp. 1–9, Mar. 2023.

[3] V. Gali, P. K. Jamwal, N. Gupta, and A. Kumar, "An adaptive dynamic power management approach for enhancing operation of microgrid with grid ancillary services," Renew. Energy, vol. 219, pp. 1–20, Dec. 2023.

[4] J. Jiang, S. Peyghami, C. Coates, and F. Blaabjerg, "A decentralized reliability-enhanced power sharing strategy for PV-based microgrids," IEEE Trans. Power Electron., vol. 36, no. 6, pp. 7281–7293, Jun. 2021.

[5] R. Wang, S. Jiang, D. Ma, Q. Sun, H. Zhang, and P. Wang, "The energy management of multiport energy router in smart home," IEEE Trans. Consum. Electron., vol. 68, no. 4, pp. 344–353, Nov. 2022.

[6] V. Gali, P. K. Jamwal, N. Gupta, and A. Kumar, "Multimode control strategy to improve the power quality and autonomy of PV-Wind-BESS based microgrid using harmonic frequency adaptive observer filter," Elect. Power Syst. Res., vol. 225, pp. 1–15, Dec. 2023.

[7] T. Vigneysh and N. Kumarappan, "Grid interconnection of renewable energy sources using multifunctional grid-interactive converters: A fuzzy logic based approach," Elect. Power Syst. Res., vol. 151, pp. 359–368, Oct. 2017.

[8] P. K. Barik, G. Shankar, and P. K. Sahoo, "Power quality assessment of microgrid using fuzzy controller aided modified SRF based designed SAPF," Int. Trans. Elect. Energy Syst., vol. 30, no. 4, pp. 1–24, 2020.

[9] S. Thakar, A. S. Vijay, and S. Doolla, "Effect of P-Q limits on microgrid reconfiguration: A capability curve perspective," IEEE Trans. Sustain. Energy, vol. 11, no. 3, pp. 2040–2048, Jul. 2020.

[10] B. Sahoo, S. K. Routray, and P. K. Rout, "Execution of adaptive transverse filter for power quality improvement," in Advances in Intelligent Computing and Communication, Singapore: Springer, 2021, pp. 409–421.

[11] D. Stojić, N. Georgijević, M. Rivera, and S. Milić, "Novel orthogonal signal generator for single phase PLL applications," Inst. Eng. Technol. Power Electron., vol. 11, no. 3, pp. 427–433, 2018.

[12] R. Zhao, S. Wu, C. Wang, H. Xu, X. Jiang, and Y. Wang, "A novel discretization method for multiple second-order generalized integrators," IEEE Trans. Power Electron., vol. 36, no. 10, pp. 10998–11002, Oct. 2021.

[13] H. Ahmed and D. Çelik, "Enhanced UPQC control scheme for power quality improvement in wave energy driven PMSG system," IEEE Trans. Energy Convers., 2024, doi: 10.1109/TEC.2024.3425954.

[14] N. Babu P, J. M. Guerrero, P. Siano, R. Peesapati, and G. Panda, "An improved adaptive control strategy in grid-tied PV system with active power filter for power quality enhancement," IEEE Syst. J., vol. 15, no. 2, pp. 2859–2870, Jun. 2021.

[15] B. Guo, S. Bacha, M. Alamir, A. Hably, and C. Boudinet, "Generalized integrator-extended state observer with applications to grid-connected converters in the presence of disturbances," IEEE Trans. Control Syst. Technol., vol. 29, no. 2, pp. 744–755, Mar. 2021.

[16] B. Singh, C. Jain, and S. Goel, "ILST control algorithm of single-stage dual purpose grid connected solar PV system," IEEE Trans. Power Electron., vol. 29, no. 10, pp. 5347–5357, Oct. 2014.

[17] S. P. Singh, D. Pathak, A. Kumar, and P. Sanjeevikumar, "An optimized fractional-order modified adaptive variable step-size LMS control approach to enhance DVR performance," IEEE Trans. Consum. Electron., vol. 70, no. 1, pp. 471–483, Feb. 2024.

[18] S. Mishra et al., "Implementation of an ADALINE-based adaptive control strategy for an LCLC-PV-DSTATCOM in the distribution system for power quality improvement," Energies, vol. 16, no. 1, pp. 1–22, 2022.

[19] S. Mittal, A. Singh, and P. Chittora, "Design and development of leaky least mean fourth control algorithm for single-phase grid-connected multilevel inverter," Int. J. Circuit Theory Appl., vol. 52, no. 1, pp. 328–345, 2024.

[20] S. J. Alam and S. R. Arya, "Volterra LMS/F based control algorithm for UPQC with multi-objective optimized PI controller gains," IEEE J. Emerg. Sel. Topics Power Electron., vol. 11, no. 4, pp. 4368–4376, Aug. 2023.

[21] V. Yadav, B. Singh, and A. Verma, "Robust control for improving performance of grid-synchronized solar PV-BES-wind based microgrid," Sustain. Energy Technol. Assess., vol. 64, pp. 1–11, Apr. 2024.

[22] M. Kashif and B. Singh, "Interactive solar water pumping unit with enhanced frequency locked loop-based synchronization for smart residential prosumers," IEEE Trans. Consum. Electron., vol. 70, no. 1, pp. 597–607, Feb. 2024.

[23] N. Mansouri, S. Nasri, A. Lashab, J. M. Guerrero, and A. Cherif, "Innovative grid-connected photovoltaic systems control based on complex-vector-filter," Energies, vol. 15, no. 18, pp. 1–14, 2022.

[24] D. Srivastava, V. Narayanan, B. Singh, and A. Verma, "A novel AWMOGI control for single stage SPVA based hybrid microgrid with smooth mode transfer capabilities," in Proc. IEEE IAS Global Conf. Emerg. Technol. (GlobConET), London, U.K., 2023, pp. 1–6.

[25] R. Aljarrah et al., "Issues and challenges of grid-following converters interfacing renewable energy sources in low inertia systems: A review," IEEE Access, vol. 12, pp. 5534–5561, 2024.

[26] M. K. Hajimahani, H. Zamani, and S. Jamali, "Data window selection for removal of decaying DC component in current phasor estimation for distance protection," Elect. Power Syst. Res., vol. 223, pp. 1–12, Oct. 2023.

[27] L. Xiong, X. Liu, C. Zhao, and F. Zhuo, "A fast and robust real-time detection algorithm of decaying DC transient and harmonic components in three-phase systems," IEEE Trans. Power Electron., vol. 35, no. 4, pp. 3332–3336, Apr. 2020.

[28] J. Mace, A. Cervone, and D. Dujic, "Self-synchronized grid impedance estimation unit using interpolated DFT technique," IEEE Trans. Power Electron., vol. 39, no. 4, pp. 4624–4635, Apr. 2024.

[29] L. Wang, Q.-S. Vo, and A. V. Prokhorov, "Stability improvement of a multimachine power system connected with a large-scale hybrid wind-photovoltaic farm using a supercapacitor," IEEE Trans. Ind. Appl., vol. 54, no. 1, pp. 50–60, 2018.

[30] Q. Zhang et al., "Average-value modeling of direct-driven PMSG-based wind energy conversion systems," IEEE Trans. Energy Convers., vol. 37, no. 1, pp. 264–273, Mar. 2022.

[31] L. Wang et al., "Grid resilience enhancement and stability improvement of an autonomous dc microgrid using a supercapacitor-based energy storage system," IEEE Trans. Ind. Appl., vol. 60, no. 2, pp. 1975–1985, 2024.

[32] G. Sahoo, R. K. Sahu, S. Panda, N. R. Samal, and Y. Arya, "Modified Harris Hawks optimization-based fractional-order fuzzy PID controller for frequency regulation of multi-micro-grid," Arabian J. Sci. Eng., vol. 48, no. 11, pp. 14381–14405, 2023.

[33] H. M. Mousavi, H. M. CheshmehBeigi, and M. Ahmadi, "A DDSRF-based VSG control scheme in islanded microgrid under unbalanced load conditions," Elect. Eng., vol. 105, no. 6, pp. 4321–4337, 2023.

[34] V. Narayanan and B. Singh, "CNISOGI and VSSMCLMS filters for solving grid and load abnormalities for a microgrid with seamless mode transfer capability," IEEE Trans. Ind. Appl., vol. 59, no. 4, pp. 4225–4237, 2023.

[35] L. Wang et al., "Grid resilience enhancement and stability improvement of an autonomous dc microgrid using a supercapacitor-based energy storage system," IEEE Trans. Ind. Appl., vol. 60, no. 2, pp. 1975–1985, Mar./Apr. 2024.